Design, Modeling, and Control of an IPMSM With an Asymmetric Rotor and Search Coils for Absolute Position Sensorless Drive

Yong-Cheol Kwon, *Student Member, IEEE*, Seung-Ki Sul, *Fellow, IEEE*, Noor Aamir Baloch, Shinya Morimoto, and Motomichi Ohto

***Abstract*—In this paper, a design methodology and control algorithms of an interior permanent-magnet synchronous machines (IPMSM) for absolute position sensorless drive are proposed. In conventional research on absolute position sensorless control, initial motion of the rotor was inevitable, which was not preferred in many applications. In order to eliminate the initial motion, an IPMSM with an asymmetric rotor and search coils is devised. In the proposed IPMSM, the information of the absolute position is included in the voltage signals at the search coils. By measuring and analyzing the search coil voltages, the absolute position can be estimated without any initial motion of the rotor. Overall performances of the proposed motor are evaluated through rigorous finite element analyses and experimental tests.**

***Index Terms*—Absolute position sensorless drive, finite element analysis (FEA), motor design, motor modeling, permanent-magnet synchronous machine (PMSM).**

NOMENCLATURE

p	Number of pole pairs.
θ_{rm}	Rotor position in mechanical angle.
θ_r	Rotor position in electrical angle, $p \cdot \theta_{rm}$.
$\hat{\theta}_{rm}$, $\hat{\theta}_r$	Estimated values of θ_{rm} and θ_r, respectively.
λ_f	Flux linkage from permanent magnets.
R_s	Stator winding resistance.
L_{ds}, L_{qs}	d and q components of synchronous inductance.
v^s_{ds}, v^s_{qs}	d and q components of stator input voltage in stationary reference frame.
v^s_{dm}, v^s_{qm}	d and q components of search coil voltage in stationary reference frame.
°E	Degrees in electrical angle (unit of angle).
°M	Degrees in mechanical angle (unit of angle).

Manuscript received February 15, 2016; revised April 14, 2016; accepted May 20, 2016. Date of publication June 7, 2016; date of current version September 16, 2016. Paper 2016-EMC-0113.R1, presented at the 2015 9th International Conference on Power Electronics and Energy Conversion Congress and Exposition (ECCE) Asia, Seoul, South Korea, June 1–5, and approved for publication in the IEEE TRANSACTIONS ON INDUSTRY APPLICATIONS by the Electric Machines Committee of the IEEE Industry Applications Society.

Y.-C. Kwon is with Department of Electrical and Computer Engineering, Seoul National University, Gwanakgu, Seoul 151742, South Korea (e-mail: dydcjfe@gmail.com).

S.-K. Sul is with the School of Electrical Engineering and Computer Science, Seoul National University, Gwanakgu, Seoul 151742, South Korea (e-mail: sulsk@plaza.snu.ac.kr).

N. A. Baloch is with Energy Conversion Technology Group, Yaskawa Electric Corporation, Kitakyushu 806-0004, Japan (e-mail: Noor.Aamir.Baloch@yaskawa.co.jp).

S. Morimoto and M. Ohto are with Yaskawa Electric Corporation, Kitakyushu 806-0004, Japan (e-mail: Shinya.Morimoto@yaskawa.co.jp; Motomichi.Ohto@yaskawa.co.jp).

Color versions of one or more of the figures in this paper are available online at http//ieeexplore.ieee.org.

Digital Object Identifier 10.1109/TIA.2016.2574991

I. INTRODUCTION

SENSORLESS control of interior permanent-magnet synchronous machines (IPMSMs) has been developed and widely used for its advantages such as reduced cost and axial length of the drive system and enhanced reliability. Sensorless control algorithms can be categorized into two groups: fundamental model based methods [1], [2] and saliency tracking methods [3]–[5]. Although the former methods exhibit reasonable performance at medium- to high-speed range, the accuracy of the rotor position estimation is degraded at zero to low-speed range, where the magnitude of back electromotive force (EMF) becomes smaller. The smaller back EMF means that the rotor position estimation becomes vulnerable to disturbances such as inverter nonlinearities and current sensing error. Saliency tracking methods [3]–[5] have been used at zero to low-speed range. Since the inductances of IPMSMs are clearly determined by the rotor position, the rotor position can be estimated by injecting additional high frequency (HF) voltage signal and analyzing its resultant HF current ripple.

Although there has been a lot of research conducted into sensorless control so far, estimation of the absolute (mechanical) rotor position has been rarely considered. In most conventional research [1]–[5], the rotor position only in electrical angle (θ_r), not in mechanical angle (θ_{rm}), was estimated. The following equation addresses the relation between θ_r and θ_{rm}:

$$\theta_r = p \cdot \theta_{rm}. \tag{1}$$

Since θ_r is normally bounded between –180°E and 180°E, θ_{rm} cannot be uniquely determined from the information of θ_r except in the case of $p = 1$. Although the information of θ_r is enough in normal applications which only require the torque/speed control, in some applications, such as control of robot arms and machine tools, the absolute rotor position (θ_{rm}) should be identified and controlled. In usual ac motors, their inductances are repeated per every electrical revolution ($\theta_r = 2\pi$), which makes it difficult to identify θ_{rm}. Thus, modification of the basic motor design is essential for the absolute rotor position estimation.

In [6] and [7], IPMSM designs with nonuniform winding and an asymmetric rotor were proposed. Thanks to the stator and rotor asymmetries, the inductances are not repeated like the case of

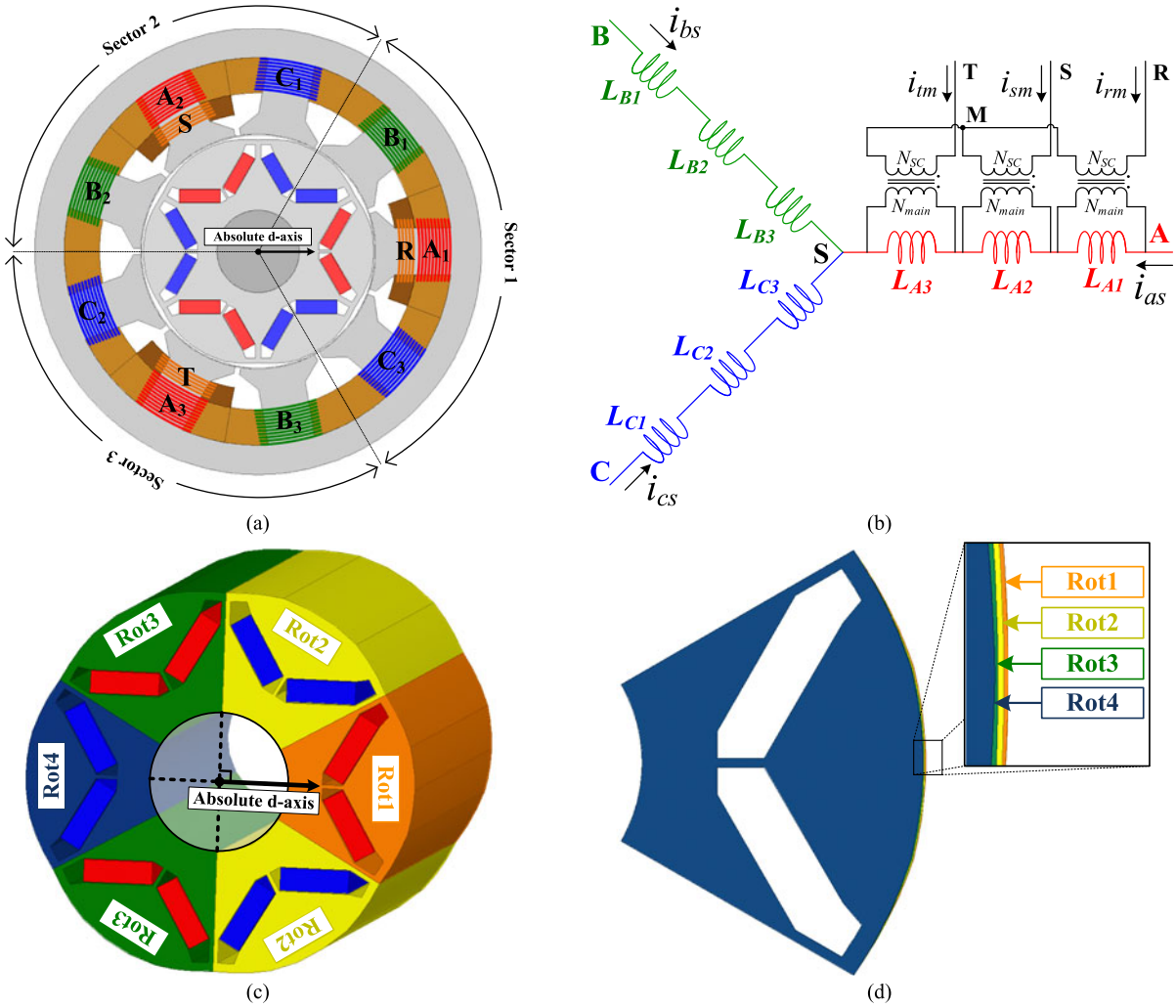

Fig. 1. Proposed motor design. (a) Cross-sectional diagram. (b) Winding configuration. (c) Assembly of rotor pieces. (d) Overlapped rotor pieces.

normal motors but modulated according to θ_{rm}. The modulated inductances can be reflected to HF current ripple induced by HF voltage injection. This phenomenon can be exploited for identifying θ_{rm}. However, in the designs proposed in [6] and [7], the information of θ_{rm} was measurable only at several distinct positions. Thus, the rotor had to be aligned to specific positions to get the information of θ_{rm}. This brought about undesired initial motion of the rotor which was 100°M in [6] and 30°M in [7], in the worst case. Due to this initial motion of the rotor, the application area of the methods proposed in [6] and [7] could be limited.

This paper proposes an IPMSM design for the estimation of the absolute rotor position without the initial motion of the rotor [8]. The proposed motor has an asymmetric rotor and additional search coils. Injecting HF voltage to the main winding, the information of θ_{rm} can be extracted from the voltages measured at the search coils without the initial motion of the rotor. In addition to the works addressed in [8], this paper extensively includes pulse-width modulation (PWM) techniques for the voltage measurement and basic characteristics of the proposed motor. The effectiveness of the proposed motor and control algorithms is verified through analytic approaches, finite element analyses (FEA), and experiments in sequence.

II. Proposed Method

A. Basic Structure of the Proposed Motor

In Fig. 1, the structure of the proposed motor is shown. There are two windings at the stator: main winding (ABC) that delivers power to the motor and search coil winding (RST) that is used to measure voltage. As shown in Fig. 1(a), the stator is mechanically divided into three sectors because $p = 3$. In Fig. 1(b), connection of the coils can be seen. In the proposed design, each phase of the main winding consists of series-connected three 40-turn coils and the three-phase windings are linked in *Y*-connection. The three search coils are also *Y*-connected and they form a three-phase winding. The search coils work as voltage transformers converting input voltage applied to the main winding to another three-phase voltage. The numbers of turns of the main coil and the search coil are denoted as N_{main}

TABLE I
SPECIFICATIONS OF TEMPLATE MOTOR

Rated speed	3000 r/min	λ_f	0.0625 V·s
Rated power	300 W	R_s	0.49 Ω
Rated current	$2.85\,A_{rms}$	L_{ds}	7.13 mH
p	3	L_{qs}	11.04 mH

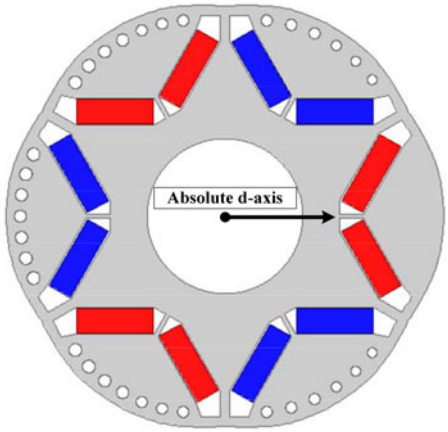

Fig. 2. Another candidate for rotor design: Rotor with holes.

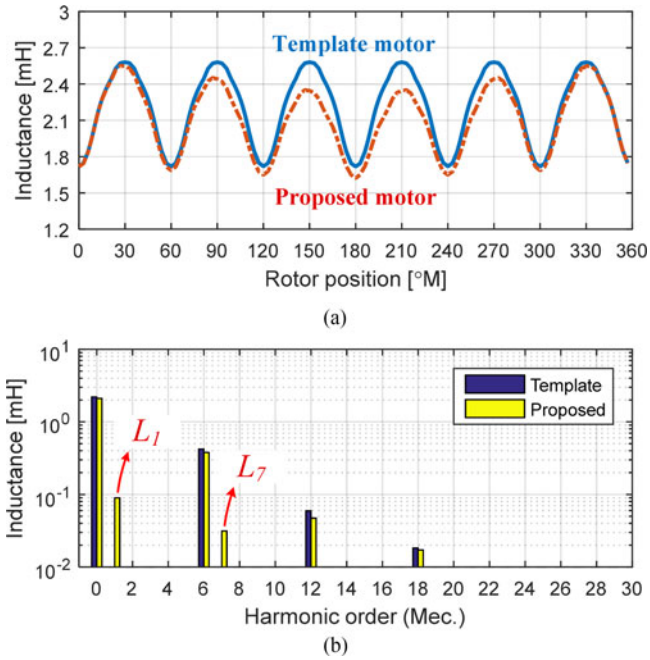

Fig. 3. FEA: (a) self-inductances of template and proposed motors; and (b) their harmonic spectra.

and N_{SC}, respectively. The structure of the proposed motor is modified from a template motor, an IPMSM with symmetric rotor and without the search coils, whose parameters are listed in Table I.

In Fig. 1(c) and (d), the structure of the rotor is shown. The rotor consists of four rotor pieces named as Rot1–Rot4. As shown in Fig. 1(d), the surface of each rotor piece is slightly shaved with different depth. This means that each rotor piece has different airgap between the stator and the rotor. For this reason, the rotor which is an assembly of the rotor pieces provokes a distinctive feature in the inductance. Although an ideal IPMSM has only 2*p*th order saliency, the proposed motor has additional first-order saliency coming from the shaved rotor. Dimension of the shaving is determined so that self- and mutual inductances of the proposed motor can have additional sinusoidal components with a period of $\theta_{rm} = 2\pi$, i.e., $L_1 \cos(\theta_{rm} + \phi)$.

Compared to the motor design in [7], there is a compromise that the search coils are used in the proposed motor in order to remove the initial motion of the rotor. Of course, the insertion of the search coils and using an additional cable give rise to extra cost and reliability issues. However, the proposed method can still be advantageous in comparison to using an absolute position sensor in terms of the volume and cost. The search coils are very thin that they do not make the motor bulky, whereas position sensors increase the axial length of the motor. Considering the cost, the search coil is relatively cheaper than position sensors. Moreover, a low-bit (such as 6-bit) ADC can be used for the measurement of the search coil voltage, which means that the voltage sensing part can be also cheaper than a resolver-to-digital converter (RDC) needed to drive a resolver.

Instead of the shaved rotor, a rotor with many holes near the surface of it, shown in Fig. 2, can also be used. In the figure, it is shown that the size of each hole gradually varies according to the mechanical angle. As discussed in [7], such holes in the rotor can induce saturation band near the surface of the rotor, which brings on a similar effect of increased airgap. However, after FEA and experimental verification of the rotor with holes, it was concluded that it is even more difficult to get desirable inductance profile from the holes than the shaving. From the perspective of manufacturing, the shaved rotor is also easier to construct. So, only the shaved rotor is considered in this paper.

B. Modeling of the Proposed Motor

Due to the shaving of the rotor, the inductance profile according to θ_{rm} is slightly changed. Fig. 3 shows L_{a1a1}, which is incremental self-inductance of A_1 coil extracted from FEA simulation. In current-driven simulation mode, small variation of coil current is applied and the inductance is calculated by

$$L_{a1a1} = \Delta\lambda_{as1}/\Delta i_{as1} \tag{2}$$

where λ indicates flux linkage and Δ means deviation of a quantity. In Fig. 3(a), L_{a1a1} of the proposed motor and that of the template motor are shown. It can be clearly seen that L_{a1a1} of the proposed motor contains additional first-order component. Fig. 3(b) compares harmonic spectra of L_{a1a1} of the two motors. As shown in the figure, there are only DC and multiples of 2*p*th (sixth) order harmonic components in the template motor. However, there are additional first- and seventh-order components, i.e., L_1 and L_7, in the case of the proposed motor due to the shaving of the rotor.

Now it is necessary to analyze the effect of L_1 and L_7 on basic characteristics and sensorless control. In order to do it, an

analytical model of the proposed motor will be derived. Before considering the search coils, self- and mutual inductances of the main winding can be expressed as a function of θ_{rm}. The inductances can be thought as sums of many frequency components. For example, self-inductance of A_1 coil in Fig. 3(a) can be expressed as

$$L_{a1a1} = \sum_{\mathbf{n}=0}^{\infty} L_n \cos\left(n\theta_{rm} + \phi_n\right). \tag{3}$$

Note that *n* in (3) is the harmonic order on the basis of mechanical angle. Considering magnetic coupling between coils, *n*th order flux linkages of the main coils can be represented as (4). In the case of the proposed motor, *p* equals three since it is a six-pole machine. In (4), as shown at the bottom of the page, there is an underlying assumption that flux linkage of a coil is affected only by the currents flowing through the coil itself and other two coils nearby. The phases of the inductances in (4) are intuitively derived from the geometrical structure of the proposed motor. In (4), k_n can be given by (5), which is derived from the feature that fluxes passing through a coil should definitely be linked to its two adjacent coils because magnetic flux should always be continuous

$$k_n = -\frac{1}{2\cos\frac{n}{3p}\pi}. \tag{5}$$

Considering series connection of coils in each phase and *Y* connection of ABC phases, *n*th order inductances of ABC phases can be deduced as (6) as shown at the bottom of the page, where *a* is an arbitrary integer. Total inductance can be expressed as

$$\mathbf{L_{abcs}} = \mathbf{L_{ls}} + \sum_{\mathbf{n}=0}^{\infty} \mathbf{L_{abcsn}} \tag{7}$$

where $[\,\lambda_{as}\ \lambda_{bs}\ \lambda_{cs}\,]^T = \mathbf{L_{abcs}}[\,i_{as}\ i_{bs}\ i_{cs}\,]^T$. It is worth noting that only the harmonic inductance with its harmonic order equal to zero or a multiple of *p* can be seen from the main winding. In the case of the proposed motor where $p = 3$, 1, and 7 are not multiples of *p*. That is, L_1 and L_7 cannot be seen from the main terminal, which implies that basic characteristics of the proposed motor such as torque ripple and harmonics in back EMF are rarely influenced by the rotor shaving.

In the case of ideal IPMSMs that contain only zero and 2*p*th order inductances, the inductance matrix in (7), as shown at the bottom of the page, becomes (8), where $L_{\mathrm{A}} = p{\cdot}L_0$ and $L_{\mathrm{B}} = p{\cdot}L_{2\mathrm{p}}$. Eq. (8) is the general inductance model of ideal IPMSMs that is addressed in many textbooks [9], [10].

Considering the effect of the search coils, the voltages at the search coils can be derived as follows. Since the search coil is

$$\begin{bmatrix} \lambda_{as1n} \\ \lambda_{bs1n} \\ \lambda_{cs1n} \\ \bullet \\ \bullet \\ \bullet \\ \lambda_{aspn} \\ \lambda_{bspn} \\ \lambda_{cspn} \end{bmatrix} = L_n \begin{bmatrix} \cos n\theta_{rm} & k_n\cos n\left(\theta_{rm}-\frac{1}{3p}\pi\right) & 0 & 0 & \bullet & 0 & 0 & 0 & k_n\cos n\left(\theta_{rm}+\frac{1}{3p}\pi\right) \\ k_n\cos n\left(\theta_{rm}-\frac{1}{3p}\pi\right) & \cos n\left(\theta_{rm}-\frac{2}{3p}\pi\right) & k_n\cos n\left(\theta_{rm}-\frac{3}{3p}\pi\right) & 0 & \bullet & 0 & 0 & 0 & 0 \\ 0 & k_n\cos n\left(\theta_{rm}-\frac{3}{3p}\pi\right) & \cos n\left(\theta_{rm}-\frac{4}{3p}\pi\right) & \bullet & \bullet & 0 & 0 & 0 & 0 \\ 0 & 0 & k_n\cos n\left(\theta_{rm}-\frac{5}{3p}\pi\right) & \bullet & \bullet & 0 & 0 & 0 & 0 \\ \bullet & \bullet & \bullet & \bullet & \bullet & \bullet & \bullet & \bullet & \bullet \\ 0 & 0 & 0 & 0 & \bullet & \bullet & k_n\cos n\left(\theta_{rm}+\frac{7}{3p}\pi\right) & 0 & 0 \\ 0 & 0 & 0 & 0 & \bullet & \bullet & \cos n\left(\theta_{rm}+\frac{6}{3p}\pi\right) & k_n\cos n\left(\theta_{rm}+\frac{5}{3p}\pi\right) & 0 \\ 0 & 0 & 0 & 0 & \bullet & 0 & k_n\cos n\left(\theta_{rm}+\frac{5}{3p}\pi\right) & \cos n\left(\theta_{rm}+\frac{4}{3p}\pi\right) & k_n\cos n\left(\theta_{rm}+\frac{3}{3p}\pi\right) \\ k_n\cos n\left(\theta_{rm}+\frac{1}{3p}\pi\right) & 0 & 0 & 0 & \bullet & 0 & 0 & k_n\cos n\left(\theta_{rm}+\frac{3}{3p}\pi\right) & \cos n\left(\theta_{rm}+\frac{2}{3p}\pi\right) \end{bmatrix} \begin{bmatrix} i_{as1} \\ i_{bs1} \\ i_{cs1} \\ \bullet \\ \bullet \\ \bullet \\ i_{asp} \\ i_{bsp} \\ i_{csp} \end{bmatrix}. \tag{4}$$

$$\mathbf{L_{abcsn}} = \begin{cases} p\cdot L_n \begin{bmatrix} \cos a\theta_r & -k_n\cos a\left(\theta_r-\frac{1}{3}\pi\right) & -k_n\cos a\left(\theta_r+\frac{1}{3}\pi\right) \\ -k_n\cos a\left(\theta_r-\frac{1}{3}\pi\right) & \cos a\left(\theta_r-\frac{2}{3}\pi\right) & -k_n\cos a\left(\theta_r+\frac{3}{3}\pi\right) \\ -k_n\cos a\left(\theta_r+\frac{1}{3}\pi\right) & -k_n\cos a\left(\theta_r+\frac{3}{3}\pi\right) & \cos a\left(\theta_r+\frac{2}{3}\pi\right) \end{bmatrix} & \text{for } n = a\cdot p \\ \begin{bmatrix} 0\,0\,0 \\ 0\,0\,0 \\ 0\,0\,0 \end{bmatrix} & \text{otherwise} \end{cases} \tag{6}$$

only for the voltage measurement, there is almost zero current in the search coil ($\mathbf{i}_{\mathrm{rstm}} = 0$). Then nth order components of flux linkages of A-phase main coils can be written as

$$\begin{bmatrix} \lambda_{as1n} \\ \lambda_{as2n} \\ \lambda_{as3n} \end{bmatrix} = \mathbf{L_{asn}} \cdot \begin{bmatrix} i_{as} \\ i_{bs} \\ i_{cs} \end{bmatrix} \tag{9}$$

where equation is shown at the bottom of the page.

The flux linkages of A-phase main coils can be expressed as

$$\begin{bmatrix} \lambda_{as1} \\ \lambda_{as2} \\ \lambda_{as3} \end{bmatrix} = \frac{1}{3} \begin{bmatrix} L_{ls} \\ L_{ls} \\ L_{ls} \end{bmatrix} i_{as} + \sum_{n=0}^{\infty} \mathbf{L_{asn}} \cdot \begin{bmatrix} i_{as} \\ i_{bs} \\ i_{cs} \end{bmatrix} + \frac{1}{3}\lambda_f \begin{bmatrix} \cos\theta_r \\ \cos\theta_r \\ \cos\theta_r \end{bmatrix}. \tag{10}$$

In Fig. 1(a), RST coils are wound close to the main coils so that they are magnetically well-coupled with A-phase coils. So, flux linkages of RST coils can be deduced as

$$\begin{bmatrix} \lambda_{rm} \\ \lambda_{sm} \\ \lambda_{tm} \end{bmatrix} = \frac{N_{SC}}{N_{main}} \left(\begin{bmatrix} \lambda_{as1} \\ \lambda_{as2} \\ \lambda_{as3} \end{bmatrix} - \frac{1}{3} \begin{bmatrix} L_{ls} \\ L_{ls} \\ L_{ls} \end{bmatrix} i_{as} \right)$$

$$= \frac{1}{3}\lambda_f \frac{N_{SC}}{N_{main}} \begin{bmatrix} \cos\theta_r \\ \cos\theta_r \\ \cos\theta_r \end{bmatrix} + \frac{N_{SC}}{N_{main}} \sum_{n=0}^{\infty} \mathbf{L_{asn}} \cdot \begin{bmatrix} i_{as} \\ i_{bs} \\ i_{cs} \end{bmatrix}. \tag{11}$$

Transforming (11) into stationary dq coordinate quantities

$$\begin{bmatrix} \lambda_{dm}^s \\ \lambda_{qm}^s \end{bmatrix} = \frac{N_{SC}}{N_{main}} \sum_{n=0}^{\infty} \mathbf{T_{dq}} \mathbf{L_{asn}} \frac{3}{2} \mathbf{T_{dq}}^{\mathbf{T}} \begin{bmatrix} i_{ds}^s \\ i_{qs}^s \end{bmatrix}. \tag{12}$$

In (12), $\mathbf{T}_{\mathrm{dq}}$ indicates the transformation matrix defined as

$$\mathbf{T_{dq}} \triangleq \frac{2}{3} \begin{bmatrix} 1 & -1/2 & -1/2 \\ 0 & \sqrt{3}/2 & -\sqrt{3}/2 \end{bmatrix}. \tag{13}$$

$\mathbf{T_{dq}} \mathbf{L_{asn}} \frac{3}{2} \mathbf{T_{dq}}^{\mathbf{T}}$ in (12) reduces to (14) after some algebraic manipulation

$$\mathbf{T_{dq}} \mathbf{L_{asn}} \frac{3}{2} \mathbf{T_{dq}}^{\mathbf{T}}$$

$$= \begin{cases} \begin{bmatrix} 0 & 0 \\ 0 & 0 \end{bmatrix} & \text{for } n = 3a \\ L_n \begin{bmatrix} \frac{3}{2}\cos n\theta_{rm} - \frac{\sqrt{3}}{2}\tan\frac{1}{9}n\pi \cdot \cos\left(n\theta_{rm} - \frac{\pi}{2}\right) \\ \frac{3}{2}\sin n\theta_{rm} - \frac{\sqrt{3}}{2}\tan\frac{1}{9}n\pi \cdot sin\left(n\theta_{rm} - \frac{\pi}{2}\right) \end{bmatrix} & \text{for } n = 3a+1 \\ L_n \begin{bmatrix} \frac{3}{2}\cos n\theta_{rm} - \frac{\sqrt{3}}{2}\tan\frac{1}{9}n\pi \cdot \cos\left(n\theta_{rm} - \frac{\pi}{2}\right) \\ -\frac{3}{2}\sin n\theta_{rm} \frac{\sqrt{3}}{2}\tan\frac{1}{9}n\pi \cdot sin\left(n\theta_{rm} - \frac{\pi}{2}\right) \end{bmatrix} & \text{for } n = 3a+2 \end{cases} \tag{14}$$

where a is an arbitrary integer.

As specified in (14), zero and multiples of $2p$th order inductances that determine the fundamental inductances expressed in (8) have no impact on the search coil voltage. However, L_1 and L_7 that cannot be seen from the main terminal can be seen from the search coil terminal since they are in the case of $n = 3a+1$ in (14). Assuming that L_1 and L_7 components are added to an ideal IPMSM represented in (8), flux linkages of the search coils stationary dq coordinate can be expressed as

$$\begin{bmatrix} \lambda_{dm}^s \\ \lambda_{qm}^s \end{bmatrix} = \frac{N_{SC}}{N_{main}} \sum_{n=1,7} \mathbf{T_{dq}} \mathbf{L_{asn}} \frac{3}{2} \mathbf{T_{dq}}^{\mathbf{T}} \begin{bmatrix} i_{ds}^s \\ i_{qs}^s \end{bmatrix}. \tag{15}$$

From $[\, v_{dm}^s \; v_{qm}^s \,]^T = d/dt \cdot [\, \lambda_{dm}^s \; \lambda_{qm}^s \,]^T$, the search coil voltage in stationary reference frame $\mathbf{v_{dqm}^s}$ is deduced as

$$\mathbf{L_{asn}} = L_n \begin{bmatrix} \cos n\theta_{rm} & k_n \cos n\left(\theta_{rm} - \frac{1}{9}\pi\right) & k_n \cos n\left(\theta_{rm} + \frac{1}{9}\pi\right) \\ \cos n\left(\theta_{rm} - \frac{6}{9}\pi\right) & k_n \cos n\left(\theta_{rm} - \frac{7}{9}\pi\right) & k_n \cos n\left(\theta_{rm} - \frac{5}{9}\pi\right) \\ \cos n\left(\theta_{rm} + \frac{6}{9}\pi\right) & k_n \cos n\left(\theta_{rm} + \frac{5}{9}\pi\right) & k_n \cos n\left(\theta_{rm} + \frac{7}{9}\pi\right) \end{bmatrix}.$$

$$\mathbf{L_{abcs}} = \mathbf{L_{ls}} + \mathbf{L_{abcs0}} + \mathbf{L_{abcs2p}}$$

$$= \begin{bmatrix} L_{ls} + L_A + L_B\cos 2\theta_r & -\frac{1}{2}L_A + L_B\cos 2\left(\theta_r - \frac{\pi}{3}\right) & -\frac{1}{2}L_A + L_B\cos 2\left(\theta_r + \frac{\pi}{3}\right) \\ -\frac{1}{2}L_A + L_B\cos 2\left(\theta_r - \frac{\pi}{3}\right) & L_{ls} + L_A + L_B\cos 2\left(\theta_r + \frac{\pi}{3}\right) & -\frac{1}{2}L_A + L_B\cos 2\theta_r \\ -\frac{1}{2}L_A + L_B\cos 2\left(\theta_r + \frac{\pi}{3}\right) & -\frac{1}{2}L_A + L_B\cos 2\theta_r & L_{ls} + L_A + L_B\cos 2\left(\theta_r - \frac{\pi}{3}\right) \end{bmatrix} \tag{8}$$

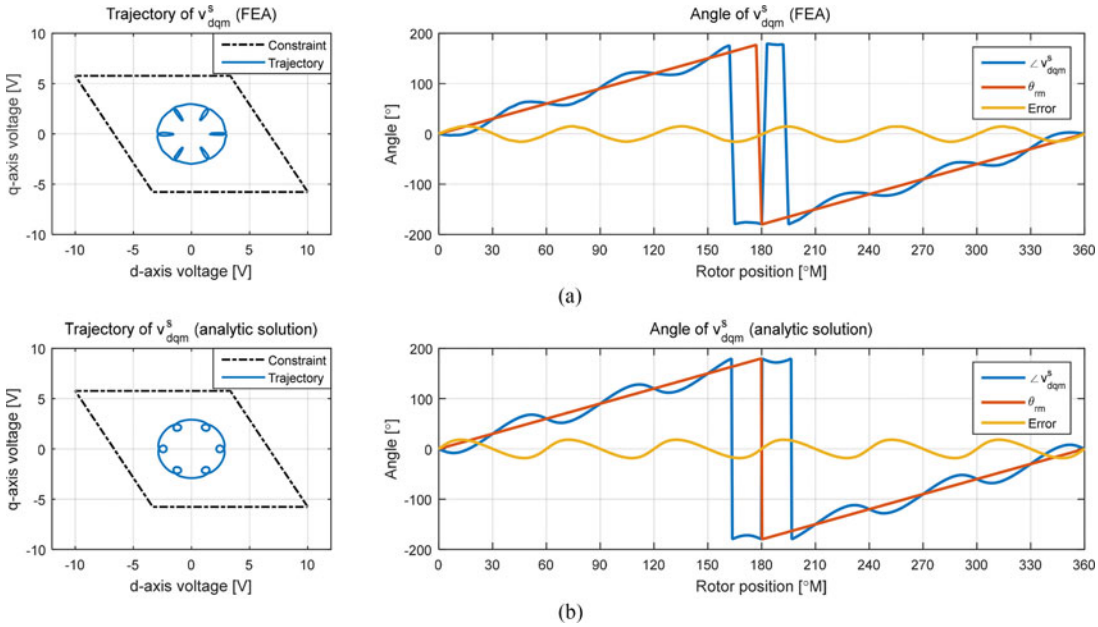

Fig. 4. Trajectory and angle of $\mathbf{v^s_{dqm}}$ from (a) FEA simulation and (b) analytic solution in (16).

$$\begin{bmatrix} v^s_{dm} \\ v^s_{qm} \end{bmatrix} = K_{SC} \sum_{n=1,7} \left\{ \begin{array}{l} \sqrt{3} L_n \left(\Sigma L_s - \Delta L_s \cos 2\theta_r \right) \begin{bmatrix} \cos n\theta_{rm} \\ \sin n\theta_{rm} \end{bmatrix} + \\ \\ L_n \Delta L_s \sin 2\theta_r \cdot tan\frac{1}{9} n\pi \begin{bmatrix} \cos\left(n\theta_{rm} - \frac{\pi}{2}\right) \\ sin\left(n\theta_{rm} - \frac{\pi}{2}\right) \end{bmatrix} \end{array} \right\} v^s_{ds}. \tag{16}$$

Some constants in (16) are defined as

$$\Sigma L_s \triangleq \frac{L_{ds} + L_{qs}}{2}, \ \Delta L_s \triangleq \frac{L_{ds} - L_{qs}}{2}$$

and

$$K_{SC} \triangleq \frac{\sqrt{3}}{2} \frac{N_{SC}}{N_{main}} \frac{1}{L_{ds} L_{qs}}. \tag{17}$$

v^s_{qs} is neglected in (16) since the injection voltage is applied only at *d*-axis ($v^s_{qs} = 0$) in the absolute position estimation process. The voltage term in (16) clearly contains the information of $\theta_{\rm rm}$ in its angle.

In Fig. 4, trajectory and angle of $\mathbf{v^s_{dqm}}$ according to the absolute position calculated from FEA and from the analytic solution in (16) are shown. Fig. 4(a) is derived from voltage-driven simulation. Applying PWM voltage pulse to the main terminal, the induced voltage at the search coil terminal is taken and used to construct the voltage trajectory. For the analytic one in Fig. 4(b), v^s_{ds} is set as 207 V, which is two thirds of $V_{\rm DC}$. Trajectory and angle of v^s_{dqm} calculated from (16), well match to FEA results, which proves the validity of (16). Small differences between Fig. 4(a) and (b) come from small errors in the model in (4) and that harmonic inductances other than L_1 and L_7 are neglected in (16). Clear correlation between $\angle \mathbf{v^s_{dqm}}$ and $\theta_{\rm rm}$ visualized in Fig. 4 can be utilized for the estimation of the absolute position.

Magnetic saturation in the motor is not considered in the modeling procedure from (3) to (15). If there is magnetic saturation, inductance formation in (4) would be changed. However, the absolute position estimation is used only at the initial startup where load is usually not applied and no magnetic saturation can be presumed.

C. Estimation of the Absolute Rotor Position

In Fig. 5, block diagram of the proposed absolute position sensorless drive system including the voltage measurement part is shown. The inverter feeds the proposed motor through the main terminal and the search coil terminal is linked directly to an analog-to-digital converter (ADC) in a control board. Basic sensorless control algorithm is based on the square-wave injection method [5] with some modification. Because the *dq* components of $\mathbf{v^s_{dqm}}$ in (16) are independent of the zero-sequence component, it is enough to measure line-to-line voltages to obtain v^s_{dm} and v^s_{qm}. Thus, only $v_{\rm rt}$ and $v_{\rm st}$ are measured by the ADC. From the measured $v_{\rm rt}$ and $v_{\rm st}$, $\mathbf{v^s_{dqm}}$ can be calculated as

$$\mathbf{v^s_{dqm}} = \begin{bmatrix} v^s_{dm} \\ v^s_{qm} \end{bmatrix} = \begin{bmatrix} 2/3 & -1/3 \\ 0 & 1/\sqrt{3} \end{bmatrix} \begin{bmatrix} v_{rt} \\ v_{st} \end{bmatrix}. \tag{18}$$

Since ADC has an input range, $v_{\rm rt}$ and $v_{\rm st}$ should be properly limited within the input range of ADC. Using an ADC with ± 10 V input range, the constraints of v^s_{dm} and v^s_{qm} are

$$-\sqrt{3} v^s_{dm} - \frac{20}{\sqrt{3}} \le v^s_{qm} \le -\sqrt{3} v^s_{dm} + \frac{20}{\sqrt{3}}$$

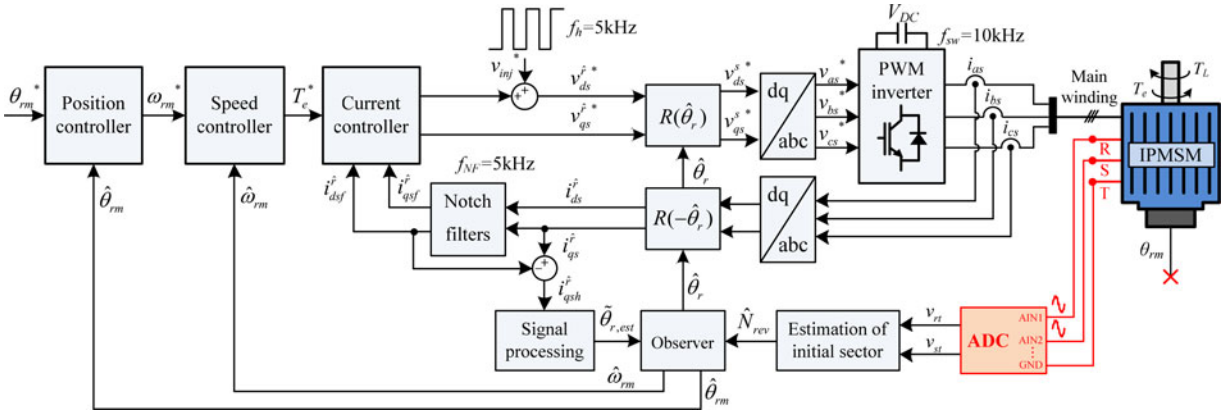

Fig. 5. Block diagram of proposed absolute position sensorless drive system.

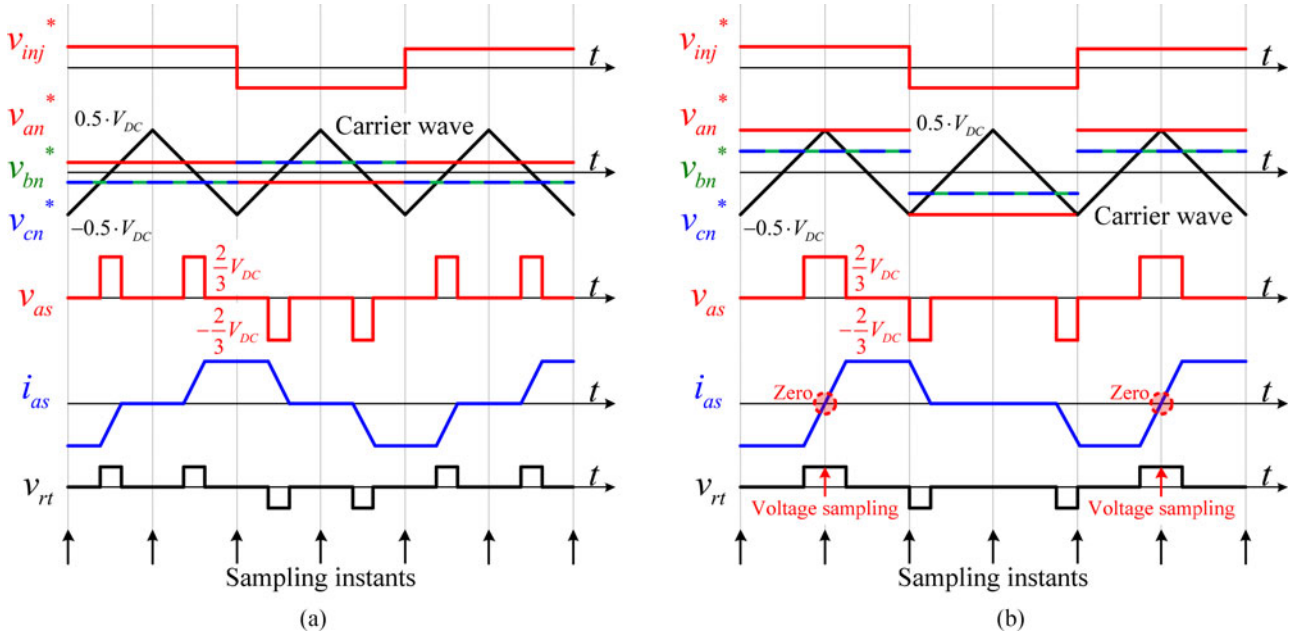

Fig. 6. Typical waveforms during signal injection with (a) SCPWM and (b) DPWM.

$$-\frac{10}{\sqrt{3}} \le v_{qm}^{s} \le \frac{10}{\sqrt{3}}. \tag{19}$$

The constraint specified in (19) has a parallelogram shape in stationary dq coordinate plane as shown in Fig. 4.

Fig. 6 describes typical waveforms under HF voltage injection based on carrier-based PWM implementation [11]. Two popular PWM methods, namely symmetrical continuous PWM (SCPWM) and discontinuous PWM (DPWM), are compared in the figure. Three-phase pole voltage references $\mathbf{v}_{\mathrm{abcn}}{}^{*}$ are calculated from injection voltage reference, $v_{\mathrm{inj}}{}^{*}$. Pulses of v_{as} are generated from the comparison of $\mathbf{v}_{\mathrm{abcn}}{}^{*}$ and the carrier wave. The current i_{as} varies according to v_{as}. As expressed in (16), $\mathbf{v}_{\mathbf{dqm}}^{\mathbf{s}}$ is proportional to the input voltage at the main winding. Thus, v_{rt} is proportional to v_{as} as shown in Fig. 6.

In order to properly measure v_{rt} and v_{st}, SCPWM cannot be used. As shown in Fig. 6(a), v_{rt} and v_{st} are zero at sampling instants because the effective vector is located in the middle of sampling period. So v_{rt} and v_{st} cannot be measured using SCPWM. Using DPWM, v_{rt} and v_{st} become nonzero at one out of four sampling instants, which make it possible to sample v_{rt} and v_{st} at that instant. Also, it is very helpful that i_{as} becomes zero at that instant. Because inductances in the expression of $\mathbf{v}_{\mathbf{dqm}}^{\mathbf{s}}$ in (16) are influenced by magnetic saturation, it is desirable that i_{as} is zero when v_{rt} and v_{st} are sampled. For these reasons, DPWM is temporarily used when measuring v_{rt} and v_{st}. In normal operation, SCPWM is used for reduced current harmonics to the motor.

From the measured v_{rt} and v_{st}, initial absolute position can be estimated. Estimated value of the absolute rotor position can be expressed as

$$\hat{\theta}_{rm} = \frac{1}{p}\left(\hat{\theta}_r + 2\pi \cdot \hat{N}_{rev}\right) \tag{20}$$

where $\hat{N}_{rev}$ stands for a count of rotor revolution in electrical angle. In the basic sensorless control, only $\hat{\theta}_r$ can be estimated. $\hat{N}_{rev}$ should be estimated to get $\hat{\theta}_{rm}$.

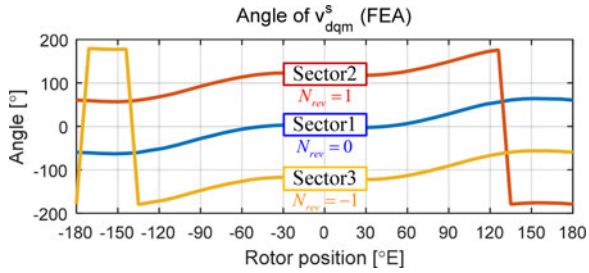

Fig. 7. FEA: $\angle \mathbf{v}^{\mathbf{s}}_{\mathbf{dqm}}$ according to rotor position.

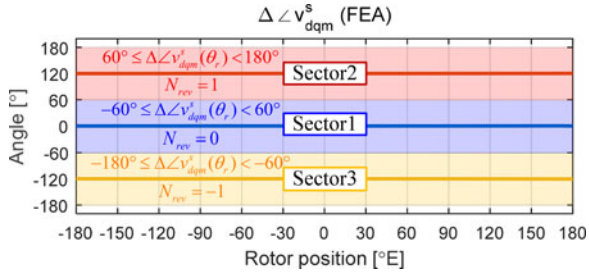

Fig. 8. FEA: $\Delta\angle \mathbf{v}^{\mathbf{s}}_{\mathbf{dqm}}(\theta_r)$ according to rotor position.

If $\angle \mathbf{v}^{\mathbf{s}}_{\mathbf{dqm}}$ in Fig. 4(a) is seen on the basis of electrical angle, Fig. 7 can be drawn. It is clear that $\angle \mathbf{v}^{\mathbf{s}}_{\mathbf{dqm}}$ of three sectors have similar shapes but they are 120° apart from each other. Average shape of $\angle \mathbf{v}^{\mathbf{s}}_{\mathbf{dqm}}$ can be obtained using the following manipulation which cancels the offsets

$$\angle \mathbf{v}^{\mathbf{s}}_{\mathbf{dqm\_avg}}(\theta_r) = \frac{\angle \mathbf{v}^{\mathbf{s}}_{\mathbf{dqm\,1}}(\theta_r) + \left(\angle \mathbf{v}^{\mathbf{s}}_{\mathbf{dqm\,2}}(\theta_r) - \frac{2}{3}\pi\right) + \left(\angle \mathbf{v}^{\mathbf{s}}_{\mathbf{dqm\,3}}(\theta_r) + \frac{2}{3}\pi\right)}{3} \tag{21}$$

where in $\angle \mathbf{v}^{\mathbf{s}}_{\mathbf{dqm\,x}}(\theta_r)$ subscript "x" stands for the sector number. $\angle \mathbf{v}^{\mathbf{s}}_{\mathbf{dqm\_avg}}(\theta_r)$ is calculated from an offline test and used as a reference shape of $\angle \mathbf{v}^{\mathbf{s}}_{\mathbf{dqm}}$ for the identification of $\hat{N}_{rev}$. Subtracting $\angle \mathbf{v}^{\mathbf{s}}_{\mathbf{dqm\_avg}}(\theta_r)$ from $\angle \mathbf{v}^{\mathbf{s}}_{\mathbf{dqm}}$ in Fig. 7, Fig. 8 can be derived. For easy expression, $\Delta\angle \mathbf{v}^{\mathbf{s}}_{\mathbf{dqm}}(\theta_r)$ can be defined as

$$\Delta\angle \mathbf{v}^{\mathbf{s}}_{\mathbf{dqm}}(\theta_r) \triangleq \angle \mathbf{v}^{\mathbf{s}}_{\mathbf{dqm}} - \angle \mathbf{v}^{\mathbf{s}}_{\mathbf{dqm\_avg}}(\theta_r). \tag{22}$$

If the rotor position is in sector 1, $-60° \le \Delta\angle \mathbf{v}^{\mathbf{s}}_{\mathbf{dqm}}(\theta_r) < 60°$; sector 2, $60° \le \Delta\angle \mathbf{v}^{\mathbf{s}}_{\mathbf{dqm}}(\theta_r) < 180°$; or sector 3, $-180° \le \Delta\angle \mathbf{v}^{\mathbf{s}}_{\mathbf{dqm}}(\theta_r) < -60°$. From this feature, $\hat{N}_{rev}$ can be estimated by

$$\hat{N}_{rev} = \text{round}\left(\frac{\text{BOUND\_PI}\left(\Delta\angle \mathbf{v}^{\mathbf{s}}_{\mathbf{dqm}}(\hat{\theta}_r)\right)}{\frac{2}{3}\pi}\right) \tag{23}$$

where BOUND_PI(*) stands for variable '*' bounded between –180° to 180°.

In Fig. 8, $\Delta\angle \mathbf{v}^{\mathbf{s}}_{\mathbf{dqm}}(\theta_r)$ is represented as straight lines because it comes from FEA results that are free from measurement error, manufacturing tolerance, inverter nonlinearity, etc. However, $\Delta\angle \mathbf{v}^{\mathbf{s}}_{\mathbf{dqm}}(\theta_r)$ from an experiment can vary according to θ_r. Fortunately, there is ±60° error margin in $\Delta\angle \mathbf{v}^{\mathbf{s}}_{\mathbf{dqm}}(\theta_r)$.

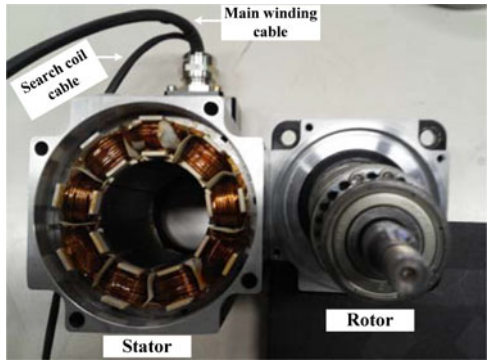

Fig. 9. Contructed prototype motor.

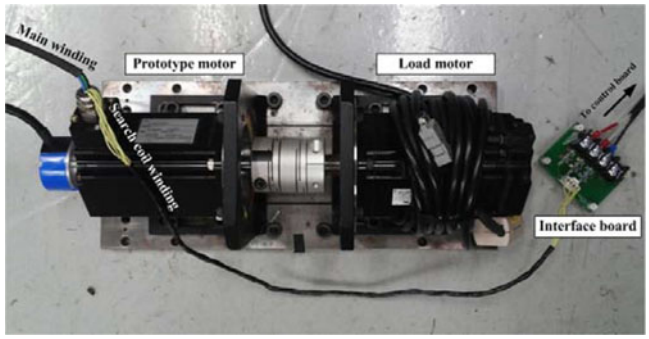

Fig. 10. Motor-generator set.

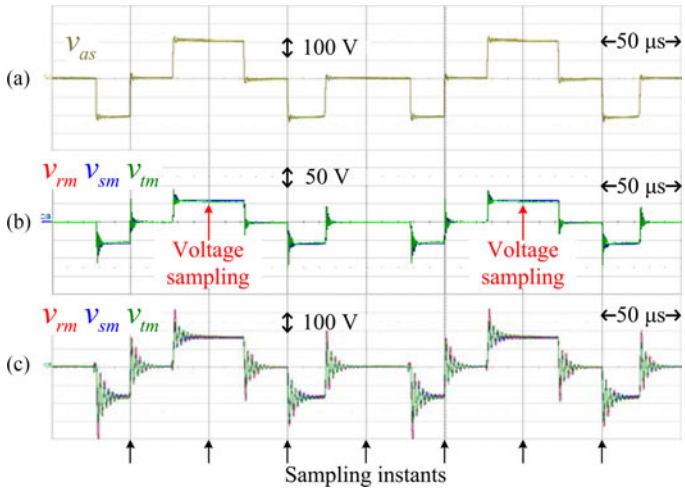

Fig. 11. Experiment: Measured (a) input voltage at main terminal and search coil voltages, (b) with NSC = 35, and (c) with NSC = 100.

III. Experimental Results

The proposed motor described in Fig. 1 is constructed as a prototype. The prototype motor is shown in Fig. 9. In Fig. 10, a motor-generator set for experimental test is shown. In addition to the main winding cable, there is search coil cable coming out

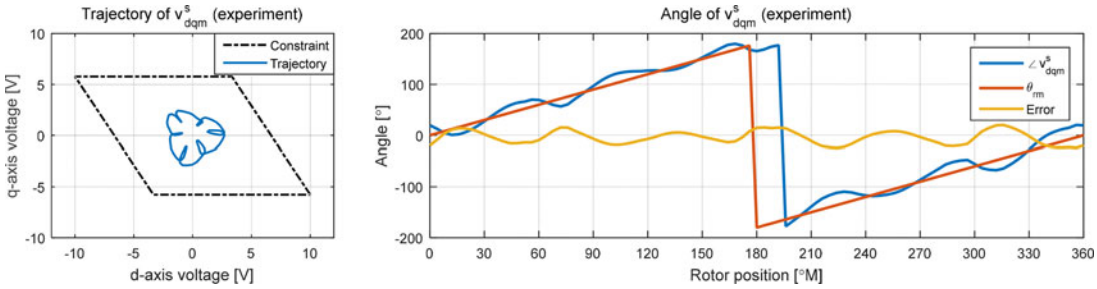

Fig. 12. Experiment: Trajectory and angle of $\mathbf{v^s_{dqm}}$.

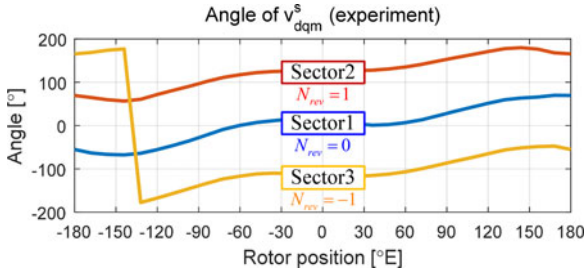

Fig. 13. Experiment: $\angle\mathbf{v^s_{dqm}}$ according to rotor position.

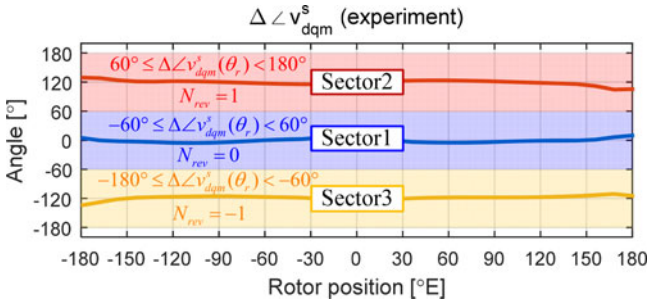

Fig. 14. Experiment: $\Delta\angle\mathbf{v^s_{dqm}}(\theta_r)$ according to rotor position.

from the prototype motor. The search coil terminal is linked to the ADC ADS8556 with six channels and 16-bit resolution. This ADC was selected for general purpose, not being selected only for the search coil voltage measurement. Because there are only three sectors, the sector identification does not require accurate information of the search coil voltage. Practically, a 6-bit ADC would be enough for this purpose.

Fig. 11 shows waveforms of the input voltage at the main winding, $v_{\rm as}$, and line-to-neutral search coil voltages, $\mathbf{v}_{\rm rstm}$, during the signal injection. DPWM is used for proper measurement of $v_{\rm rt}$ and $v_{\rm rt}$. In the figure, the waveform of $v_{\rm as}$ is in agreement with that in Fig. 6(b) and $\mathbf{v}_{\rm rstm}$ become nonzero at one out of four sampling instants. It can be found that there is oscillation in $\mathbf{v}_{\rm rstm}$. The oscillation comes from *LC* resonance due to parasitic capacitors at the search coils [12]. In order to ensure that the search coil voltages are settled down at sampling instants, the pulse of $v_{\rm as}$ should be wide enough. That is, the injection voltage should be high enough. Fig. 11(b) and (c) shows the effects of $N_{\rm SC}$ on the measured voltage of the search coil. First, the magnitude of $\mathbf{v}_{\rm rstm}$ is proportional to $N_{\rm SC}$. That is, $N_{\rm SC}$ can be used as a parameter to scale $\mathbf{v}_{\rm rstm}$. Second, the oscillation gets larger and lasts longer with higher $N_{\rm SC}$ because the parasitic capacitance at the search coil seen from the main terminal is proportional to the square of $N_{\rm SC}$. This provokes an upper limit of $N_{\rm SC}$. $N_{\rm SC} = 35$ was selected for the proposed motor for better waveforms of $\mathbf{v}_{\rm rstm}$.

In Fig. 12, trajectory and angle of $\mathbf{v^s_{dqm}}$ obtained from the experiment are shown. Compared with the FEA result in Fig. 4(a), the experimental result in Fig. 12 is slightly distorted. But as shown in Fig. 14, $\Delta\angle\mathbf{v^s_{dqm}}(\theta_r)$ has very small error, which guarantees the feasibility of the absolute position estimation algorithm in (23).

In Fig. 15, the absolute position estimation at various initial positions is demonstrated. At initial startup with sensorless control based on the signal injection, $\hat{N}_{rev}$ is assumed as zero. In every case, 300 ms is spent for taking many samples of $v_{\rm rt}$ and $v_{\rm st}$ to calculate their mean values. Because the environment of the voltage measurement can be noisy, it is required to use mean values of $v_{\rm rt}$ and $v_{\rm st}$ for the calculation of $\angle\mathbf{v^s_{dqm}}$. This time period can be tuned according to experimental environment. After 300 ms, $\hat{N}_{rev}$ can be obtained by (23). Then, the absolute position can be estimated by (20). After this procedure, it is programmed that the rotor is aligned to the absolute zero mechanical angle by position control. $Flag_{\rm APE}$ in the figure indicates that the absolute position estimation algorithm is activated. Regardless of where the rotor position is initially, the absolute rotor position can be estimated without any failure.

Fig. 16 shows the performance of absolute position control with the positive rated load torque and the negative rated load torque. After the estimation of the initial rotor position, rapidly varying position command is applied. Regardless of load condition, the absolute rotor position is quickly regulated to its command.

IV. Basic Characteristics (FEA)

Due to the shaving of the rotor, basic characteristics of the proposed motor might be changed. In Figs. 17 and 18, back EMF and torque characteristics of the proposed motor are compared with those of the template motor. These results are from FEA simulations. Compared to the case of the template motor, there are only slight changes in back EMF and torque harmonics of the proposed motor. This is distinguishing feature of the proposed motor compared to other motor designs proposed in [6] and [7], i.e., trench-type, hole-type, and shaving-type motors, which have additional low-order harmonics in their back EMF and torque. However, the fundamental component of back EMF

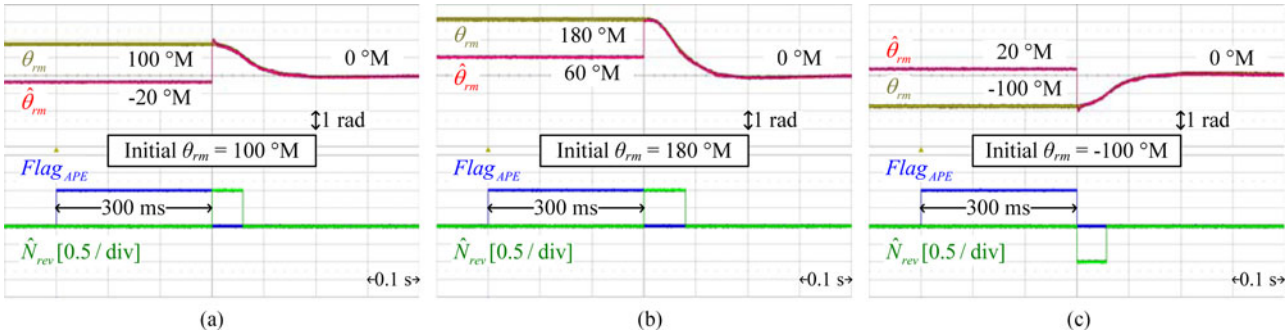

Fig. 15. Experiment: Estimation of initial absolute rotor position. Initial rotor position is set to (a) 100 °M, (b) 180 °M, and (c) –100 °M.

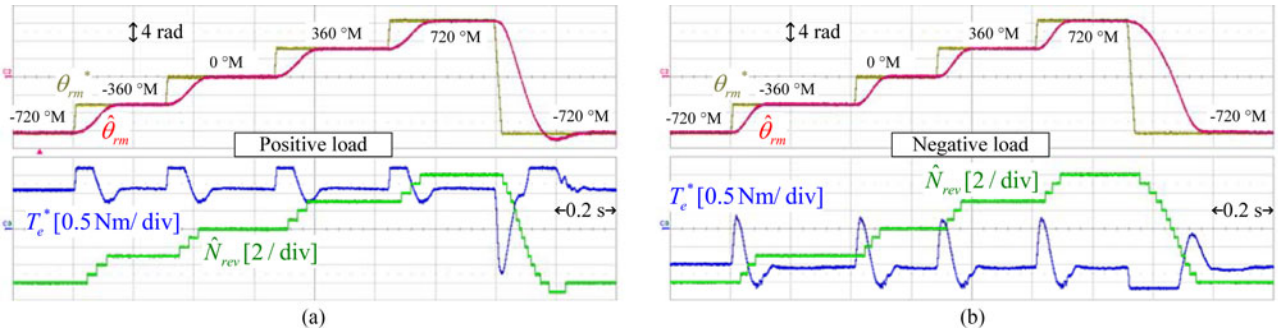

Fig. 16. Experiment: Control of absolute rotor position. (a) Positive load ($T_{\rm L} > 0$). (b) Negative load ($T_{\rm L} < 0$).

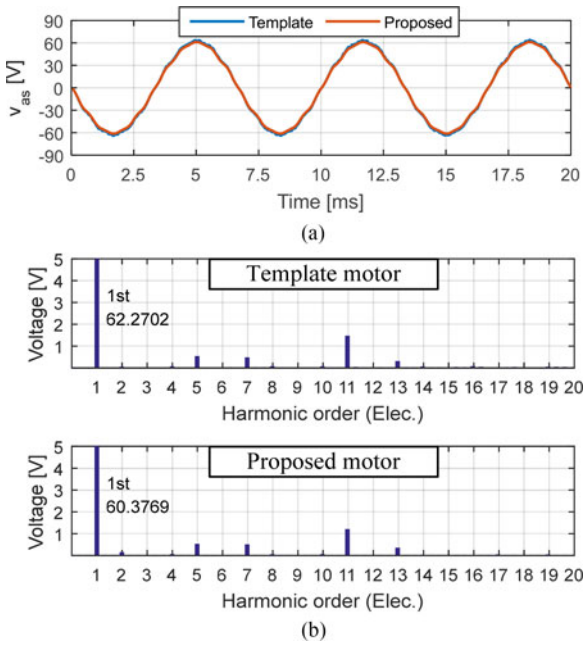

Fig. 17. FEA: (a) Waveforms and (b) harmonic spectra of back EMF.

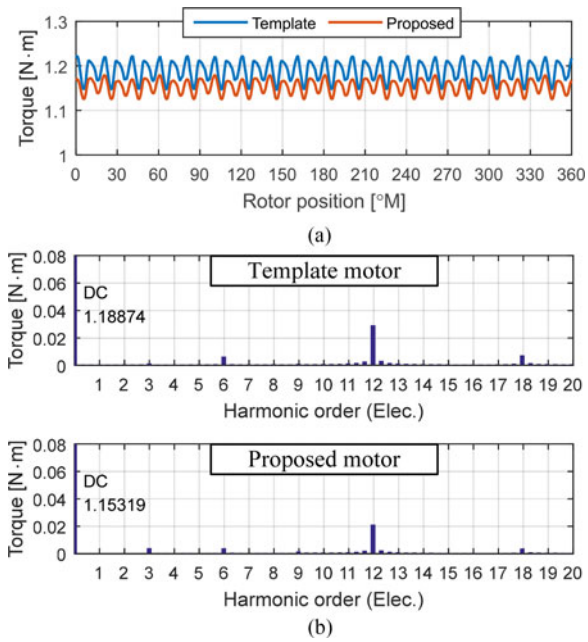

Fig. 18. FEA: (a) Waveforms and (b) harmonic spectra of torque.

and average torque are decreased by about 3% in the proposed motor.

Since the rotor of the proposed motor is designed to be asymmetric, there can be unbalanced magnetic force (UMF). In Fig. 19, magnitude and direction of UMF are shown. For the computation of UMF, Maxwell's stress tensor at the mid-airgap between the rotor and the stator is used [13]. Although the motor designs proposed in [6] and [7] have UMFs which stroke as the rotor rotates, the direction of UMF of the proposed motor follows the rotor position as shown in Fig. 19(b).

Undesirable effects such as decreased average torque and UMF are inevitable since the rotor is asymmetrically shaved. Based on the magnetic circuit analysis of IPMSMs addressed in [14], the flux generated by permanent magnets (PMs) can be

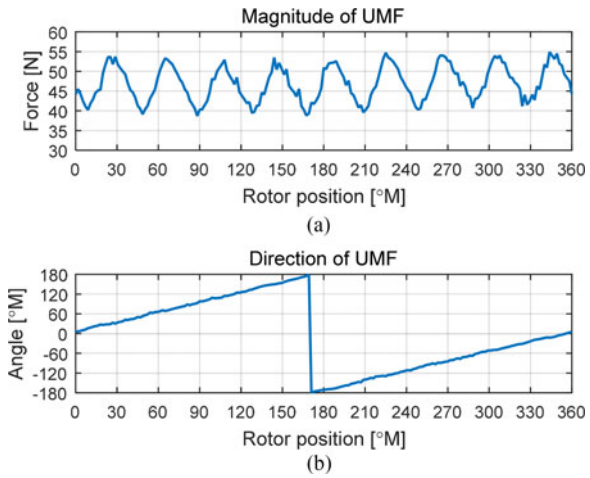

Fig. 19. FEA: (a) magnitude; and (b) direction of UMF.

expressed as

$$\Phi_{PM} = \frac{F_{PM}}{R_{PM} + R_g} \tag{24}$$

where $F_{\rm PM}$ stands for MMF generated by a PM. $R_{\rm PM}$ and $R_{\rm g}$ are reluctances of a PM and airgap, respectively. MMF drop in the core is neglected. Φ_{PM} is proportional to the PM flux linkage λ_f. From (24), it can be understood that the decrease of back EMF and torque are brought about due to increased $R_{\rm g}$ by the shaving. Letting Δg be the increment in airgap due to the shaving, variation of λ_f can be approximated as

$$\Delta\lambda_f \propto -\Delta g \tag{25}$$

because the increment of $R_{\rm g}$ by Δg is much smaller than $R_{\rm PM}$ + $R_{\rm g}$. In similar senses, it can be deduced that L_1 and the magnitude of UMF are also proportional to Δg. These relations can be summarized as

$$\begin{aligned} |\Delta\lambda_f| &= k_\lambda \cdot L_1 \\ \|F_{xy}\| &= k_F \cdot L_1 \end{aligned} \tag{26}$$

where $\|F_{xy}\|$ is average magnitude of UMF vector. Based on FEA data, $k_\lambda = 22.47$ A and $k_{\rm F} = 522.8$ kN/H. Eq. (26) claims that the undesirable effects can be alleviated if L_1 is reduced by less shaving the rotor. However, there is a limit on how small L_1 can be. Eq. (16) can be simplified as

$$\left\|\mathbf{v}^{\mathbf{s}}_{\mathbf{dqm}}\right\| \propto N_{SC} L_1 \tag{27}$$

which implies that if L_1 becomes smaller $\|\mathbf{v}^{\mathbf{s}}_{\mathbf{dqm}}\|$ can be reduced, which degrades signal-to-noise ratio (SNR) of the measured $\mathbf{v}^{\mathbf{s}}_{\mathbf{dqm}}$. It is possible to keep $\|\mathbf{v}^{\mathbf{s}}_{\mathbf{dqm}}\|$ the same by reducing L_1 and increasing $N_{\rm SC}$ simultaneously. But it should be noted that there is an upper limit of $N_{\rm SC}$ due to the oscillation issue as aforementioned. Thus, the dimension of the shaving and $N_{\rm SC}$ should be determined considering these tradeoff relations.

V. Conclusion

In this paper, an IPMSM design with an asymmetric rotor and search coils for absolute position sensorless drive has been proposed. The asymmetry of the rotor dimension is realized by the shaved rotor induces first-order inductance in mechanical angle, which is utilized in the absolute position estimation. It has been fully analyzed that the first-order inductance does not affect the basic inductance seen from the main terminal, but only affects the voltage at the search coils. Also, it has been shown that DPWM has better features than SCPWM for the measurement of the search coil voltages. From the measured voltages at the search coils under the signal injection, the absolute position could be estimated without any initial motion of the rotor. The effectiveness of the proposed IPMSM design has been verified by FEA simulations and experiments.

References

[1] N. Matsui, "Sensorless PM brushless DC motor drives," *IEEE Trans. Ind. Electron.*, vol. 43, no. 2, pp. 300–308, Apr. 1996.
[2] Z. Chen, M. Tomita, S. Doki, and S. Okuma, "An extended electromotive force model for sensorless control of interior permanent-magnet synchronous motors," *IEEE Trans. Ind. Electron.*, vol. 50, no. 2, pp. 288–295, Apr. 2003.
[3] P. L. Jansen and R. D. Lorenz, "Transducerless position and velocity estimation in induction and salient AC machines," *IEEE Trans. Ind. Appl.*, vol. 31, no. 2, pp. 240–247, Mar./ Apr. 1995.
[4] J. I. Ha and S. K. Sul, "Sensorless field-orientation control of an induction machine by high-frequency signal injection," *IEEE Trans. Ind. Appl.*, vol. 35, no. 1, pp. 45–51, Jan./Feb. 1999.
[5] Y. D. Yoon, S. K. Sul, S. Morimoto, and K. Ide, "High bandwidth sensorless algorithm for AC machines based on square-wave-type voltage injection," *IEEE Trans. Ind. Appl.*, vol. 47, no. 3, pp. 1361–1370, May/Jun. 2011.
[6] Y. C. Kwon, S. K. Sul, N. A. Baloch, S. Murakami, and S. Morimoto, "Design and control of IPMSM sensorless drive for mechanical rotor position estimation capability," *IEEE J. Emerg. Sel. Topics Power Electron.*, vol. 2, no. 2, pp. 152–158, Jun. 2014.
[7] Y. C. Kwon, S. K. Sul, N. A. Baloch, S. Murakami, and S. Morimoto, "Improved design of IPMSM for sensorless drive with absolute rotor position estimation capability," *IEEE Trans. Ind. Appl.*, vol. 52, no. 2, pp. 1441–1451, Mar./Apr. 2016.
[8] Y. C. Kwon, S. K. Sul, N. A. Baloch, S. Morimoto, and M. Ohto, "Design of IPMSM with eccentric rotor and search coils for absolute position sensorless drive," in *Proc. Int. Conf. Power Electron. ECCE Asia*, 2015, pp. 1135–1142.
[9] D. Novotny and T. Lipo, *Vector Control and Dynamics of AC Drives*. Oxford, U.K.: Clarendon, 1996.
[10] S. K. Sul, *Control of Electric Machine Drive Systems*. Hoboken, NJ, USA: Wiley, 2011.
[11] D. Chung, "Unified analysis of PWM method for three phase voltage source inverter using offset voltage," Ph.D. dissertation, Dept. Elect. Comput. Eng., Seoul Nat. Univ., Seoul, Korea, 2002.
[12] A. Massarini and M. Kazimierczuk, "Self-capacitance of inductors," *IEEE Trans. Power Electron.*, vol. 12, no. 4, pp. 671–676, Jul. 1997.
[13] G. H. Jang, J. W. Yoon, N. Y. Park, and S. M. Jang, "Torque and unbalanced magnetic force in a rotational unsymmetric brushless DC motors," *IEEE Trans. Ind. Magn.*, vol. 32, no. 5, pp. 5157–5159, Sep. 1996.
[14] N. Bianchi and T. M. Jahns, "Design, analysis and control of interior PM synchronous machines," in *Proc. IEEE IAS Conf. Rec. Annu. Meeting, Tuts. Course Notes*, Oct. 2004.

Yong-Cheol Kwon (S'11) was born in Korea in 1986. He received the B.S. and M.S. degrees in electrical engineering from Seoul National University, Seoul, Korea, in 2010 and 2012, respectively, where he is currently working toward the Ph.D. degree.

His current research interests include power electronics, design and control of electric machines, and sensorless drives.

Mr. Kwon received the IEEE Transactions on Industry Applications Second Prize Paper Award in 2015.

Seung-Ki Sul (S'78–M'87–SM'98–F'00) received the B.S., M.S., and Ph.D. degrees in electrical engineering from Seoul National University, Seoul, Korea, in 1980, 1983, and 1986, respectively.

From 1986 to 1988, he was an Associate Researcher in the Department of Electrical and Computer Engineering, University of Wisconsin, Madison, WI, USA. From 1988 to 1990, he was a Principal Research Engineer at LG Industrial Systems Company, Korea. Since 1991, he has been a Member of Faculty with the School of the Electrical and Computer Engineering, Seoul National University, where he is currently a Professor. He published more than 140 IEEE reviewed journal papers and a total of more than 330 international conference papers in the area of power electronics. He holds 14 U.S. patents, seven Japanese patents, 11 Korean patents, and has granted 38 Ph.D.s under his supervision. In 2015, he served as the President of the Korea Institute of Power Electronics, Seoul. His current research interests include control of electrical machines, electric/hybrid vehicles, electric propulsion of ship, and power conditioning system for renewables.

Dr. Sul received many Best Paper Awards from international conferences and journals including the First and Second Best Paper Awards, simultaneously, from the IEEE Transactions on Industry Applications in 2015. He was the Program Chair of IEEE Power Electronics Specialist Conference, 2006 and the General Chair of IEEE ECCE-Asia, the International Conference on Power Electronics (ICPE), 2011.

Noor Aamir Baloch received the B.Sc. (Hons.) and M.Sc. degrees in physics from the University of Karachi, Karachi, Pakistan, in 1991 and 1992, respectively; the M.S. degree in nuclear power engineering from the NED University of Engineering and Technology, Karachi, in 1995; and the Ph.D. degree in applied quantum physics and nuclear engineering from Kyushu University, Fukuoka, Japan, in 2002.

He joined Yaskawa Electric Corporation, Kitakyushu, Japan, and at present, he is a Member of Power Electronic Technology Department, Corporate Research and Development Center, Kitakyushu. His current research interests include the design and development of motor-drive control and power conversion.

Dr. Baloch is a member of the IEEE Control System Society.

Shinya Morimoto received the B.S. degree in control engineering from the Kyushu Institute of Technology, Kitakyushu, Japan, in 1990.

He joined Yaskawa Electric Corporation, Kitakyushu, in 1990, where he is currently a Manager with the Power Electronics Department, Corporate Research and Development Center. His research interests include the design and development of motor-drive control and power conversion.

Mr. Morimoto is a member of the Institute of Electrical Engineers of Japan, and the Society of Instrument and Control Engineers of Japan.

Motomichi Ohto received the B.Eng., M.Eng., and D.Eng. degrees in electrical engineering from Oita University, Oita, Japan, in 1984, 1986, and 2005, respectively.

Since 1986, he has been with Yaskawa Electric Corporation, Kitakyushu, Japan. His main research interests include technologies related to electromagnetic field analysis and electric motors.

Dr. Ohto received the Third Prize Paper Award from the Electric Machine Committee of the IEEE Industry Applications Society in 2011, and the Second Best Paper Award from the Electric Machinery Committee of the IEEE Power and Energy Society in 2015.